Supporting Information (SI Appendix)

Entropy and optimality in river deltas

Alejandro Tejedor[a], **Anthony Longjas**[a], **Douglas A. Edmonds**[b,c], **Ilya Zaliapin**[d], **Tryphon T. Georgiou**[e], **Andrea Rinaldo**[f,g], **and Efi Foufoula-Georgiou**[a]

[a]Department of Civil and Environmental Engineering, University of California, 92697 Irvine, California, USA; [b]Department of Earth and Atmospheric Sciences, Indiana University, Bloomington, IN 47405; [c]Center for Geospatial Data Analysis, Indiana University, Bloomington, IN 47405; [d]Department of Mathematics and Statistics, University of Nevada, Reno, Nevada, USA; [e]Department of Mechanical and Aerospace Engineering, University of California, 92697 Irvine, California, USA; [f]Laboratory of Ecohydrology, Ecole Polytechnique Federale Lausanne, 1015 Lausanne, Switzerland; [g]Dipartimento di Ingegneria Civile, Edile ed Ambientale, Universitá di Padova, 35131 Padova, Italy

Equivalence of the Input/output model to a Markov process

In this section, we prove the equivalence of the stationary probabilities that result from an irreducible and aperiodic discrete Markov process and the input/output model introduced in the Materials and Methods section.

Irreducible and aperiodic discrete Markov process. Let P be the transition probability matrix of a discrete Markov process which is irreducible (all the states are reachable from any state) and aperiodic (the return period to a given state can occur at different time steps),

$$P = \left\{p_{ij}\right\}_{NxN} . \quad [1]$$

P is an N x N square matrix, being N the number of states, and p_{ij} the probability of transition from state j to state i at each time step. Then, we can define a stationary probability distribution π:

$$P\pi = \pi, \quad [2]$$

where $\pi = \{\pi_i\}_{Nx1}$ is a column vector, whose entries correspond to the stationary probability distribution of each state i. Therefore, π_i are non-negative values, satisfying $\sum_{i=1}^{N} \pi_i = 1$.

For a given directed acyclic graph, such as the ones we used to represent delta channel networks, if we assume conservation of mass, the dynamics of the system can be modelled by a Markov process where the outlets of the graph are reconnected to the apex with transition probability one. Thus, the transition probability matrix is equal to the weighted adjacency matrix of the graph, W, if the entries w_{ij} corresponding to transition outlets to the apex are substituted by ones.

Equivalence of the Input/output model and Markov process solutions. We have shown in the Materials and Methods section that for a delta conceptualized as a directed acyclic graph fed from the most upstream node (apex) with a constant unit flux, we can compute the steady-state flux distribution F as:

$$F = (I - W)^{-1} \begin{pmatrix} 1 \\ 0 \\ 0 \\ \vdots \\ 0 \end{pmatrix} . \quad [3]$$

We prove in this section that the stationary distributions obtained from an irreducible and aperiodic Markov process, π, and an input/output model, F, are equivalent (up to a normalization factor). To prove this statement, we can decompose the transition probability matrix of the Markov process P as $P = W + R$, R is called the recirculation matrix and it is defined as follows:

$$R = \left\{r_{ij} = \delta_{i1}\delta_{j\{k\}}\right\}_{NxN} . \quad [4]$$

where δ represents the Kronecker delta; and therefore, all the entries of matrix R are zeros, except for the entries of the first row (apex has been indexed with $i = 1$ without loss of generality) that correspond to $\{k\}$-columns indexing the outlets.

Proof: If $F = \pi$, then F must be an eigenvector of the probability transition matrix P, and therefore $PF = F$. Given,

$$\begin{cases} F = (I - W)^{-1} \begin{pmatrix} 1 \\ 0 \\ 0 \\ \vdots \\ 0 \end{pmatrix} \\ P = W + R \end{cases} \quad [5]$$

then,

$$(W + R)(I - W)^{-1} \begin{pmatrix} 1 \\ 0 \\ 0 \\ \vdots \\ 0 \end{pmatrix} = (I - W)^{-1} \begin{pmatrix} 1 \\ 0 \\ 0 \\ \vdots \\ 0 \end{pmatrix} . \quad [6]$$

By multiplying both sides of Eq. 6 from the left by $(I - W)$,

$$(I - W)(W + R)(I - W)^{-1} \begin{pmatrix} 1 \\ 0 \\ 0 \\ \vdots \\ 0 \end{pmatrix} = \begin{pmatrix} 1 \\ 0 \\ 0 \\ \vdots \\ 0 \end{pmatrix} . \quad [7]$$

Expanding the left side of Eq. 7,

$$(I-W)W(I-W)^{-1} \begin{pmatrix} 1 \\ 0 \\ 0 \\ \vdots \\ 0 \end{pmatrix} + (I-W)R(I-W)^{-1} \begin{pmatrix} 1 \\ 0 \\ 0 \\ \vdots \\ 0 \end{pmatrix} = \begin{pmatrix} 1 \\ 0 \\ 0 \\ \vdots \\ 0 \end{pmatrix} . \quad [8]$$

Simplifying and rearranging Eq. 8,

$$W\begin{pmatrix}1\\0\\0\\\vdots\\0\end{pmatrix}+(I-W)R(I-W)^{-1}\begin{pmatrix}1\\0\\0\\\vdots\\0\end{pmatrix}=\begin{pmatrix}1\\0\\0\\\vdots\\0\end{pmatrix}, \quad [9]$$

$$(I-W)R(I-W)^{-1}\begin{pmatrix}1\\0\\0\\\vdots\\0\end{pmatrix}=(I-W)\begin{pmatrix}1\\0\\0\\\vdots\\0\end{pmatrix}, \quad [10]$$

$$R(I-W)^{-1}\begin{pmatrix}1\\0\\0\\\vdots\\0\end{pmatrix}=\begin{pmatrix}1\\0\\0\\\vdots\\0\end{pmatrix}. \quad [11]$$

Defining $B=R(I-W)^{-1}$,

$$B\begin{pmatrix}1\\0\\0\\\vdots\\0\end{pmatrix}=\begin{pmatrix}1\\0\\0\\\vdots\\0\end{pmatrix}. \quad [12]$$

Considering the structure of matrix R (see Eq. 4), then B is also a sparse matrix with the following entries:

$$B=\left\{b_{ij}\right\}_{NxN}; b_{ij}=\sum_{l=1}^{N} r_{il}(I-W)^{-1}_{lj}\delta_{1i}\delta_{l\{k\}}, \quad [13]$$

where the only non-zeros entries of the B matrix are in the first row (the apex has been indexed with $i=1$ without loss of generality). Thus, the condition needed to satisfy Eq. 13 is simply that the entry $b_{11}=1$. Therefore,

$$b_{11}=\sum_{l=1}^{N} r_{1l}(I-W)^{-1}_{l1}\delta_{l\{k\}}=\sum_{l=1}^{N}(I-W)^{-1}_{l1}\delta_{l\{k\}}=1. \quad [14]$$

In other words, the sum of the entries of the first column of $(I-W)^{-1}$ that corresponds to the outlets, $\{k\}$, must be equal to one.

Given the definition of the input/output model (see Eq. 3), the first column of $(I-W)^{-1}$ stores the values of the fluxes, F. Assuming conservation of mass, and that the input of the model is set to 1, the sum of the fluxes of the outlets must be one also, proving that the Markov model based on the idea of recirculating the flux and Input/Ouput model provide consistent stationary probability distributions.

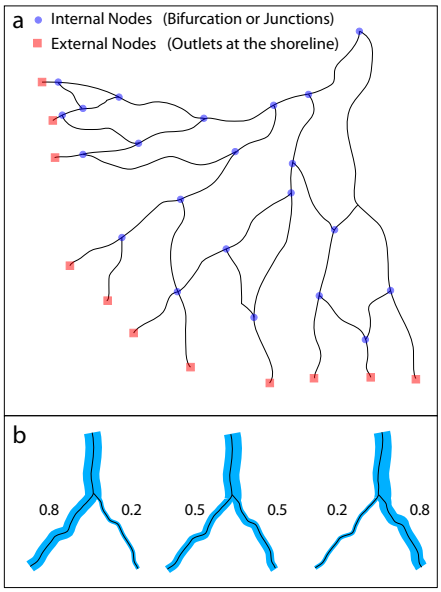

Fig. 1. Graph representation of a delta and nonlocal Entropy Rate (nER) for deltas. (a) A river delta channel network topology can be represented by a graph where channels correspond to links in the graph, and junctions and bifurcations are internal nodes (blue circles). Delta outlets are represented as external nodes (red squares). The graphs used in this paper to model delta channel networks are directed graphs (link direction corresponds to the direction of the flow in the channel) and acyclic (no cycles, i.e., water recirculation). All the information in the graph can be stored in a sparse matrix called Adjacency matrix (see text in Tejedor et al. (1) and supporting information for further details). (b) The topologic representation of a delta channel network does not contain any relevant information (besides flux directionality) about flux dynamics, and more specifically about flux partition in the bifurcations. Thus, for the same topologic configuration, such a bifurcation can exhibit very different flux partition depending on its physical attributes. Here, we use downstream channel width as a proxy of the flux partition in bifurcations. This graph representation allows us to compute algebraically different properties of the graph, including the stationary flux distribution when a constant flow input is supplied through the delta apex. One of the magnitudes that we can compute is what we define as nER. Intuitively, nER can be understood as the average amount of information (or uncertainty) needed to track packages of flux in their journey from an internal node (blue circle in a) to the outlet (red square) where it is delivered. We hypothesized that nER is maximized by delta self-organization, adjusting flux partition to maximize this uncertainty metric. To test this hypothesis, we compare the value of nER computed using channel width as proxy for flux partition, with values of nER computed when the flux partition in each bifurcation is randomized, i.e., the channel network structure (topology) is preserved but the flux partition changes at the bifurcation scale as is exemplified in b.

Physical characteristics of the ten deltas analyzed

In this section, we summarize the physical characteristics of the ten deltas selected for analysis namely: Niger, Parana, Yukon, Irrawaddy, Colville, Wax Lake, Mossy, Fraser, Danube and Mekong (Fig. 2). Extracting the channel networks from an air photo or satellite image of a delta is not an easy task. For this reason, we have adopted here for our preliminary analysis the exact five traced deltas in the study of Smart and Moruzzi (2) – Niger, Parana, Yukon, Irrawaddy, and Colville – and have added the Wax Lake and Mossy deltas for which channel networks have been extracted in previous studies (3). We also added the channel networks of Fraser, Danube and Mekong extracted from Google Earth satellite images.

Niger Delta: The Niger delta is located in the West coast of Nigeria (latitude 4.95°, longitude 6.18°). It receives input from the Niger River with an average water discharge of 6,130 m^3s^{-1} and sediment discharge of 3.97 x 10^7 tons yr^{-1} (4).

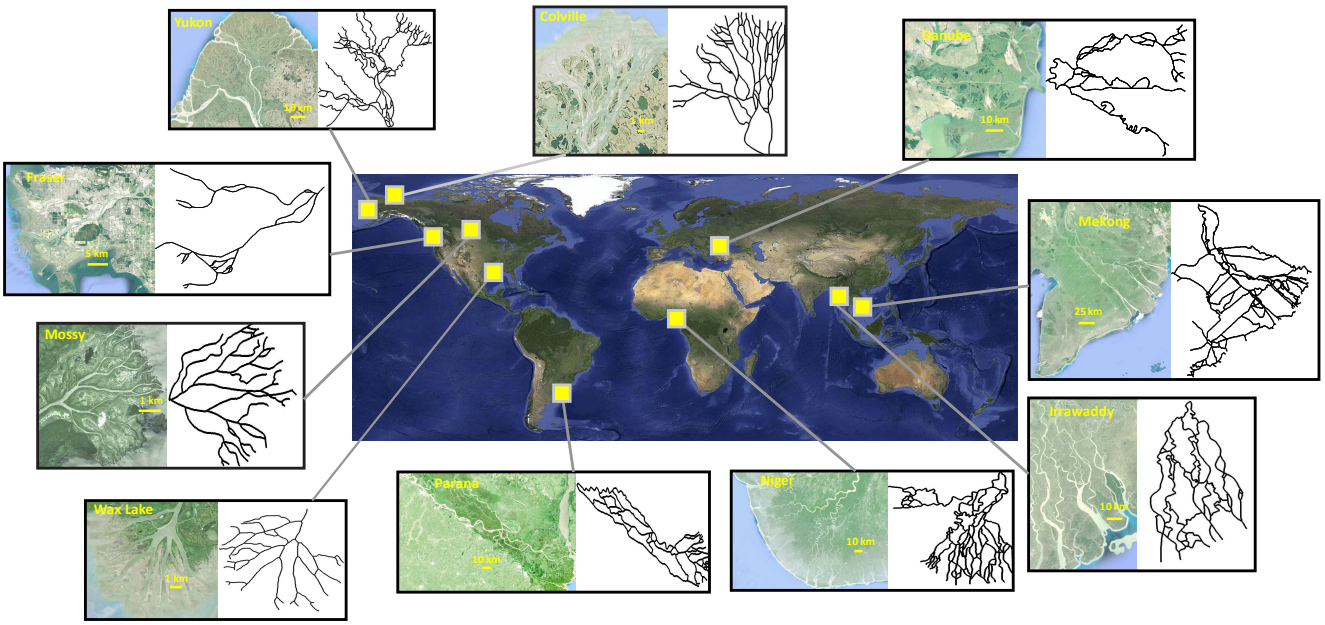

Fig. 2. Field deltas and their channel network structure. Clockwise starting from top left: Yukon, Colville, Danube, Mekong, Irrawaddy, Niger, Parana, Wax Lake, Mossy, and Fraser. Satellite images provided by Landsat/Copernicus, NASA, Digital Globe and CNES/Airbus were extracted from Google Earth. We acknowledge their respective copyrights.

Niger delta is the largest delta in Africa covering an area of 24,508 km^2, sediment is mostly fine sand (5) and the tidal range is 3.0 m. The origin of the delta is estimated to be 80 - 35 million years BP during the Late Cretaceous (6). It is classified as tide and wave dominated (4). By using the channel network extracted by Smart and Moruzzi (2), we identified 181 links, 130 vertices and 15 shoreline outlets.

Parana Delta: The Parana delta is located North of Buenos Aires, Argentina (-33.80°, -59.25°). It is fed by the Parana River, which delivers an average water discharge of 13,600 m^{3}s^{-1} and sediment discharge of 7.75 x 10^7 tons yr^{-1} (4). Parana delta covers an area of 15,463 km^2 and sediment are mostly fine sand, silt and clay (8), and the tidal range is 4.0 m. Delta genesis was estimated during the Middle Holocene (6,000 years BP) (7). It is classified as a river and geology dominated delta (4). By using the channel network extracted by Smart and Moruzzi (2), we identified 86 links, 69 vertices and 18 shoreline outlets.

Yukon Delta: The Yukon Delta, located in the West coast of Alaska, USA (63.05°, -164.05°) receives input from the Yukon River with an average water discharge of 6,620 m^{3}s^{-1} and sediment discharge of 5.97 x 10^7 tons yr^{-1} (4). It has an area covering 8,313 km^2 with mainly fine-grained sediments (10) and the tidal range is 1.5 m. Delta genesis is estimated to be during the Middle Holocene (5,000 years BP) (9). It is classified as a wave dominated delta (4). By using the channel network extracted by Smart and Moruzzi (2), we identified 169 links, 126 vertices and 24 shoreline outlets in the delta.

Irrawaddy Delta: The Irrawaddy delta is located in the Southernmost coast of Myanmar (16.20°, 95.00°). It is fed by the Irrawaddy River at an average water discharge of 13,558 m^{3}s^{-1} and sediment discharge of 2.60 x 10^8 tons yr^{-1} (4). The delta covers an area of 6,438 km^2 with the deposited sediment composed of mostly mixed mud and silt (5), and the tidal range is 4.2 m. It is estimated that the delta began to form around 8,000-7,000 years BP together with most of the deltas in Southeast Asia (11). It is classified as a tide dominated delta (4). By using the channel network extracted by Smart and Moruzzi (2), we identified 100 links, 71 vertices and 6 shoreline outlets in the delta.

Colville Delta: The Colville delta, located in the Northern part of Alaska, USA (70.40°, -150.65°), receives input from the Colville River with an average water discharge of 491.7 m^{3}s^{-1} (5) and sediment discharge of 1.16 x 10^8 tons yr^{-1} (12). With an area of 240 km^2, it is relatively small compared to other polar deltas. Sediment is mostly composed of gravel and sand (5). The tidal range is 0.2 m. The delta began to develop during the Middle Holocene (4,000 years BP) (13). It is classified as a river dominated delta (4). By using the channel network extracted by Smart and Moruzzi (2), we identified 140 links, 107 vertices and 20 shoreline outlets in the delta.

Wax Lake Delta: The Wax Lake delta, located in the coast of Louisiana, USA (29.51°, -91.44°), receives input from the Wax Lake outlet, a channel that was dredged in the early 1940s to mitigate flooding risk in the nearby Morgan City, at an average water discharge of 2,900 m^{3}s^{-1} and sediment discharge of 2.35 x 10^7 tons yr^{-1} (14). The slope of the Wax Lake delta from the delta apex to the Gulf of Mexico is 5.8 x 10^{-5} (15). Subaerial land only developed after the 1970s flood and has been experiencing rapid growth in the last two decades doubling to more than 100 km^2 today (16, 17). Sediment deposit in the delta is composed of approximately 67% sand (16), and the tidal range is 0.40 m (18). It is classified as a river dominated delta. We utilized the outline of the Wax Lake delta channel network processed by Edmonds et al. (3) containing 59 links, 56 vertices and 24 shoreline outlets.

Mossy Delta: The Mossy delta is located in Saskatchewan, Canada (54.07°, -102.35°). It is fed by the Mossy River with an average water discharge of 300 m^3s^{-1}(3) and sediment discharge of 2.20 x 10^6 tons yr^{-1} (19). The delta was formed as a result of the avulsion of the Saskatchewan River in the 1870s (20). Progradation of the delta resulted in an area of 14 km^2 in the early 1940s (19) and after the construction of a spillway dam in the 1960s, the delta ever since slowly evolved with a current area of approximately 17 km^2. Sediment in the delta is roughly 50% fine-grained sand (3). Since the delta drains into a lake (Lake Cumberland), the effect of tides is insignificant. It is classified as a river dominated delta. We have extracted the channel network of Mossy delta and identified 67 links, 61 vertices and 23 shoreline outlets.

Danube Delta: The Danube delta is located in Romania (45.2°, 29.4°) and receives input from the Danube River with an average water discharge of 6,420 m^3s^{-1} and sediment discharge of 6.72 x 10^7 tons yr^{-1} (4). It has an area of 6,468 km^2. Main control of the delta is waves (southern part) although the northern part is river-dominated (21). Recent studies show that the intensification of land use in the watershed as the population increased and land use technology has increased sedimentation in the delta (22).

Fraser Delta: The Fraser delta is located in Canada (49.18°, -122.95°) and receives input from the Fraser River with an average water discharge of 3,560 m^3s^{-1} and sediment discharge of 2.00 x 10^7 tons yr^{-1} (4). It has an area of 876 km^2. Main control of the delta is river and tide. Recent studies show that the delta is experiencing more human intervention.

Mekong Delta: The Mekong delta is located in Vietnam (10.1°, 150.6°) and receives input from the Mekong River with an average water discharge of 14,770 m^3s^{-1} and sediment discharge of 1.60 x 10^7 tons yr^{-1} (4). It has an area of 91,789 km^2. Main control of the delta is river and wave.

Delft3D Numerical Simulations

We use Delft3D to simulate the self-formed evolution of delta distributary networks. Delft3D is a physics-based morphodynamic model that has been validated for morphodynamics applications (23). We employ the depth-averaged version of Delft3D, which solves the unsteady shallow water equations in the horizontal dimension and assumes hydrostatic pressure in the vertical. Specifically, in this paper, we use model runs from Caldwell and Edmonds (24), which simulate a sediment-laden river entering a standing body of water that is devoid of waves, tides, and buoyancy forces. The river has an upstream water discharge boundary condition (steady flow of 1000 m^3s^{-1}) and carries sediment fluxes in equilibrium with the flow field. The downstream water surface boundary conditions are fixed at sea level. The flow field is coupled to the sediment transport equations (25, 26) and bed surface equations so it dynamically evolves in response to sediment transport gradients. The incoming sediment consists of grain sizes, D, lognormally distributed with a median size, D_{50}, and standard deviation $\sigma(\phi)$ (in ϕ space, where $\phi = \log_2 D$). We note that cohesiveness (defined as the percent of sediment with grain size $D \leq D_c$ = 0.064 mm) and dominant grain size (D_{84}) can be uniquely determined as a function of D_{50} and $\sigma(\phi)$ when the sediment size is lognormally distributed. Notice that other variables that can affect directly or indirectly the bulk cohesion of the system (e.g., vegetation, flow variability, and spatial heterogeneities from apex to shoreline) have not been considered here. Specifically, we compare six runs where the only difference is the median of the incoming grain size distributions D_{50}, while the standard deviation is fixed to $\sigma(\phi) = 1$. The distributions have median sizes of 0.01 mm, 0.05 mm, 0.1 mm, 0.25 mm, 0.5 mm, and 1 mm, respectively (Fig. 3). These simulations are identical to runs B1a1, B1c1, B1e1, B1h1, B1m1, and B1o1 in Table 2 of Caldwell and Edmonds (24), exploring the whole range of cohesiveness (from 0% to 100%) and values of dominant grain size from 0.014 to 1.896 mm. For more discussion on the morphodynamics of these deltaic simulations, see Caldwell and Edmonds (24).

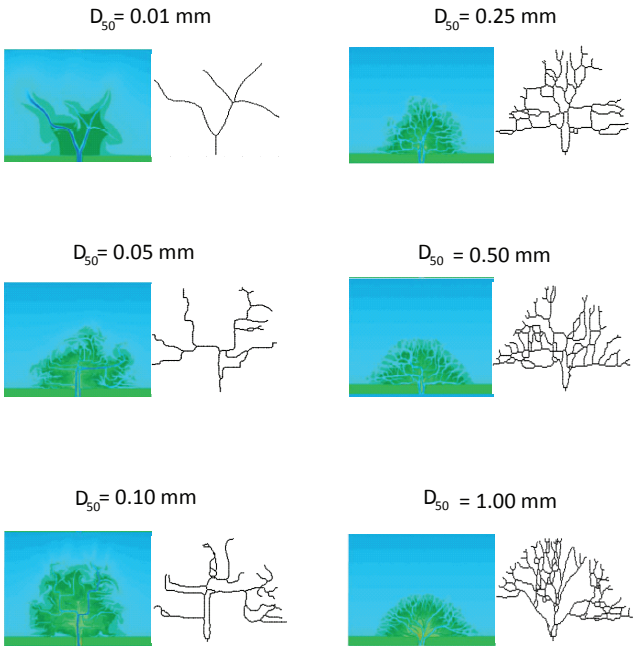

Fig. 3. Numerical deltas and their channel network structure. Six river dominated deltas (no wave or tidal energy) are displayed where the only difference is the median of the incoming grain size distributions D_{50} = 0.01 mm, 0.05 mm, 0.10 mm, 0.25 mm, 0.50 mm, and 1.00 mm.

We utilized the capability of numerical simulations to investigate the change in nER during an avulsion cycle. Fig. 4 shows the avulsion cycle analyzed in this paper obtained from the run with D_{50} = 0.10 mm.

Channel Network Extraction and Analysis. The analysis conducted in this paper relies on spectral graph theory, which requires transforming each delta channel network into a graph. Graphs are mathematical objects composed of vertices and edges. For delta channel networks, the edges represent channels, and vertices correspond to the locations where one channel splits into new channels (bifurcation) or two or more channels merge into a single channel (junction). In pre-processing the gridded data produced by the simulations, we perform the following steps:

1. Classify pixels as Land/Channels/Ocean: First, we define a shoreline with the opening angle method (27) on a binarized image where bed elevations below sea level were considered water and above sea level were considered land. We use an opening angle of 70°. All pixels not within

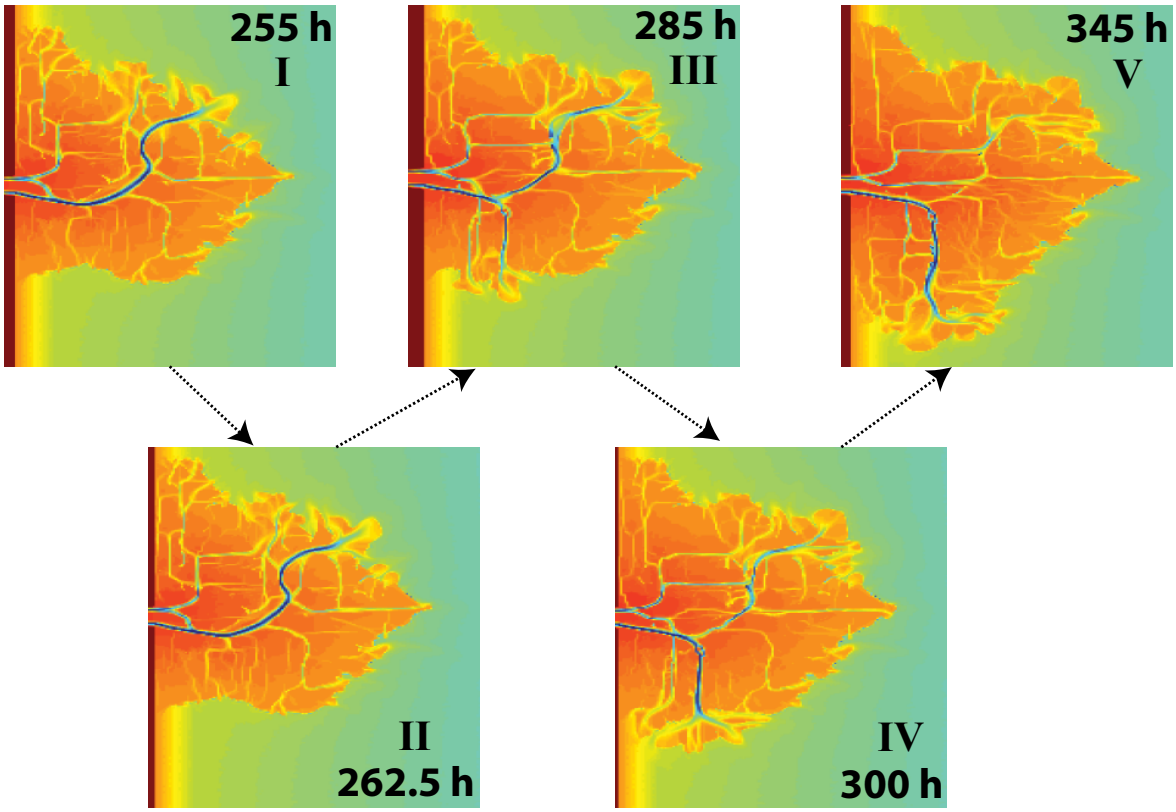

Fig. 4. Avulsion cycle. Five instances in an avulsion cycle of a Delft3D simulated delta where the main channel shifts, draining from the left (I) to the right (V) part of the delta shoreline. Intermediate stages of the avulsion cycle are also displayed: (II) the new path is created, (III) fluxes are equally divided between both paths, and (IV) the new path carries most of the flux. Top (bottom) panels are characterized by high (low) nER. Each panel is labelled with its corresponding time of simulation in hours (1 hr = 7.3 days morphodynamic time).

the shoreline are defined as ocean. Within the enclosed shoreline, pixels are defined as channels if depth > 0.25 m, velocity > 0.2 m s^{-1}, and sediment transport rate $>$ 2.25 x 10^5 m^{3}s^{-1}. Everything else within the shoreline is defined as land.

2. Eliminate disconnected channels: From all the channel pixels, we only consider those ones that belong to channel pathways that eventually drain from the apex to the shoreline, removing isolated pixels and paths.

3. Extract skeleton network: We use an algorithm (28) to define the centerline of each channel, taking into account that channels can have a large range of variation in widths (from one pixel to several). From the resulting skeleton structure and flow directions, we define the vertices and edges that uniquely determine the directed graph corresponding to the delta channel network [e.g., see Tejedor et al. (1), Figure 7].

4. Compute adjacency matrix: All information about the network connectivity can be stored in a sparse matrix called adjacency matrix. The element of the matrix a_{ij} is different from zero if the vertex j is directly connected to downstream vertex i, and zero otherwise.

5. Extract channel widths: The width of channels measured directly downstream of each bifurcation is stored and used as a proxy for flux partition [see Tejedor et al. (1), section 2.2].

1. Tejedor A, Longjas A, Zaliapin I, Foufoula-Georgiou E (2015) Delta channel networks: 1. A graph-theoretic approach for studying connectivity and steady state transport on deltaic surfaces. *Water Resour Res* 51:3998–4018.
2. Smart J, Moruzzi V (1971) Quantitative properties of delta channel networks. *Technical Report 3, IBM Thomas J. Watson Research Center* pp 1–27.
3. Edmonds D, Paola C, Hoyal D, Sheets B (2011) Quantitative metrics that describe river deltas and their channel networks. *J Geophys Res* 116:F04022.
4. Syvitski J, Kettner A, Correggiari A, Nelson B (2005) Distributary channels and their impact on sediment dispersal. *Mar Geol* 222–223:75–94.
5. Orton G, Reading H (1993) Variability of deltaic processes in terms of sediment supply with particular emphasis on grain size. *Sedimentology* 40:475–512.
6. Goudie A (2005) The drainage of Africa since the Cretaceous. *Geomorphology* 67:437–456.
7. Politis G, Bonomo M, Castineira C, Blasi A (2011) Archaeology of the upper delta of the Parana river (Argentina): Mound construction and anthropic landscapes in the Los Tres Cerros locality. *Quat Int* 245:74–88.
8. Fossati M, Cayocca F, Piedra-Cueva I (2014) Fine sediment dynamics in the Rio de la Plata. *Adv Geosci* 39:75–80.
9. Nelson H, Creager J (1977) Displacement of Yukon derived sediment from Bering sea to Chukchi sea during holocene times. *Geology* 5:141–146.
10. Walker H (1998) Arctic deltas. *J Coastal Res* 14:718–738.
11. Hedley P, Bird M, Robinson R (2010) Evolution of the Irrawaddy delta region since 1850. *Geogr J* 176:138–149.
12. Arnborg L, Walker H, Peippo J (1967) Suspended load in the Colville river, Alaska, 1962. *Geogr Ann* 49:131–144.
13. Jorgenson M, Shur Y, Walker H (2010) *Evolution of a permafrost-dominated landscape on the Colville River Delta, Northern Alaska* eds. Lewkowicz A, Allard M. (Quebec, Canada), pp 523–529.
14. Roberts H, Coleman J, Bentley S, Walker N (2003) An embryonic major delta lobe: A new generation of delta studies in the Atchafalaya-Wax lake delta system. *Gulf Coast Assoc Geol Soc Trans* 53:690–703.
15. Wagner W, et al. (2017) Elevation change and stability on a prograding delta. *Geophys Res Lett* 44:1786–1794.
16. Roberts H, Walker N, Cunningham R, Kemp G, Majersky S (1997) Evolution of sedimentary

architecture and surface morphology: Atchafalaya and Wax lake deltas, Louisiana (1973-1994). *Gulf Coast Assoc Geol Soc Trans* 47:477–484.
17. Paola C, et al. (2011) Natural processes in delta restoration: Application to the Mississippi delta. *Annu Rev Mar Sci* 3:67–91.
18. Shaw J, Mohrig D, Whitman S (2013) The morphology and evolution of channels on the Wax lake delta, Louisiana, USA. *J Geophys Res Earth Surf* 118:1562–1584.
19. Oosterlaan S, Meyers M (1995) *Evolution of the Mossy Delta in Relation to Hydrodam Construction and Lake Level Fluctuation*. (University of Illinois, Chicago), p 31.
20. Smith N, Slingerland R, Perez-Arlucea M, Morozova G (1998) The 1870s avulsion of the Saskatchewan river. *Can J Earth Sci* 35:453–466.
21. Bhattacharya J, Giosan L (2003) Wave-influenced deltas: geomorphological implications for facies reconstruction. *Sedimentology* 50:187–210.
22. Giosan L, Constantinescu S, Filip F, Deng B (2013) Maintenance of large deltas through channelization: Nature vs. humans in the Danube delta. *Anthropocene* 1:35–45.
23. Lesser G, Roelvink J, van Kester J, Stelling G (2004) Development and validation of a three-dimensional morphological model. *Coastal Eng* 51:883–915.
24. Caldwell R, Edmonds D (2014) The effects of sediment properties on deltaic processes and morphologies: A numerical modeling study. *J Geophys Res Earth Surf* 119:961–982.
25. Van Rijn L (1984) Sediment transport: Part I, Bed load transport. *J Hydraul Eng* 110:1431–1456.
26. Van Rijn L (1984) Sediment transport: Part II, Suspended load transport. *J Hydraul Eng* 110:1613–1641.
27. Shaw J, Wolinsky M, Paola C, Voller V (2008) An image-based method for shoreline mapping on complex coasts. *Geophys Res Lett* 35:L12405.
28. Lam L, Lee SW, Suen C (1992) Thinning methodologies — a comprehensive survey. *IEEE Trans Pattern Anal Mach Intell* 14:869–885.